Three-dimensional Wireless Measurement of Float–Sink Object Motions in a Gas–Solid Fluidized Bed

Tomoki Katayama [a], Yoko Otsuka [a], Shiori Saito [a], Shusaku Harada [a,*], Takuya Tsuji [b] and Jun Oshitani [c]

[a] Division of Sustainable Resources Engineering, Faculty of Engineering, Hokkaido University, N13-W8 Sapporo, Hokkaido 060-8628, Japan

[b] Department of Mechanical Engineering, Osaka University, 2-1 Yamada-oka, Suita, Osaka 565-0871, Japan

[c] Department of Applied Chemistry, Okayama University of Science, 1-1 Ridai-cho, Kita-ku, Okayama 700-0005, Japan

* Corresponding author: Shusaku Harada
Phone/Fax: + (81)-11-7066310
E-mail address: harada@eng.hokudai.ac.jp

ABSTRACT

We developed a Lagrangian sensor system capable of wirelessly measuring the 3D motions of objects and applied it to examine the floating and sinking behaviors in a gas–solid fluidized bed. The system consisted of a sensor particle, comprising a 9-axis sensor and a wireless module integrated into a spherical outer shell, and three pairs of magnetic coils. By utilizing this system, we can non-invasively measure the 3D motions of objects, which cannot be observed from the outside. In this study, we examined the motions of objects with various densities in the gas–solid fluidized bed. We found the similarity and dissimilarity between the float–sink motions of objects in fluidized beds and those in liquids. The experimental results revealed that the vertical motion of an object in the fluidized bed depends on its density and can be categorized into two distinct states: floating near the surface or settling down at the bottom. However, within a specific range of object densities close to the apparent density of the fluidized bed, the object exhibited complicated motions in the bed. In such cases, slight density variations induced unpredictable changes between the floating and sinking states. The results also suggested that the settling velocity of the objects in the fluidized bed varies with their vertical positions in the bed.

Keywords: Fluidized bed, Non-invasive measurement, Float–sink motion, Lagrangian sensor

1. Introduction

Gas–solid fluidized beds are widely employed in various engineering processes, such as drying, combustion, and catalytic reactions, in chemical and mechanical engineering fields (Kunii and Levenspiel, 1991). On the other hand, the fluid-like behavior of fluidized beds has attracted much physical interest in recent years (Soria-Verdugo et al., 2011; Fotovat et al., 2014; Chen et al., 2019; Chen et al., 2019). It is well-known that the fluidized state of media particles in fluidized beds varies depending on the particle size, density, and air-inlet velocity in a complex manner. The fluidization degree of particles is sometimes expressed by the granular temperature, which is defined by the mean-square velocity of the particles, analogous to molecular motion (Goldhirsch, 2003). Generally, the granular temperature in a fluidized bed is not uniform and depends on the flow conditions. Consequently, the fluidization state varies locally, i.e., with bubble formation or channel-like air penetration (Geldart, 1973). The overall motion of a fluidized bed is often compared to fluid motion. However, the variance of local fluidization state in the bed may cause the dissimilarity to pure fluid motion.

Fluid-like behavior of fluidized beds can be observed not only in a dynamically fluidized state, but also in a pseudo-static state. At air velocities near the minimum fluidization velocity, the mass of the media particles balances the air-permeation resistance, causing the particles to exist in a pseudo-zero gravity state. In this case, a pressure gradient is formed almost linearly inside the fluidized bed. This hydrostatic-like pressure gradient exerts a “buoyant” force on the objects immersed in the fluidized bed. Consequently, float–sink phenomena occur in the bed similar to those in liquids. Recently, dry separation techniques have been proposed to take advantage of these fluid-like behaviors of gas–solid fluidized beds for ore separation in arid regions (Oshitani et al., 2013; Oshitani et al., 2013).

In the above-mentioned fluidization state, the buoyant force is proportional to the apparent density of the fluidized bed (the density of the media particles including the void region) in an ideal state. Therefore, the objects with a density lower than the apparent density of the media particles float near the surface, whereas the objects with a higher density sink to the bottom in principle. Recently, however, the dissimilarity between the float–sink phenomena in fluidized beds and those in liquids has been attracting attention (Oshitani et al., 2016; Penn et al., 2017; Tsuji et al., 2021). For example, incomprehensible float–sink reverse motions have been observed in response to slight variations in the density of objects (Oshitani et al., 2016). Complicated motions depending on the object shape or air-inlet velocity have also been observed (Tsuji et al., 2022; Oshitani et al., 2023; Uemoto et al., 2023). These phenomena never occur in liquids and are observed only in gas–solid fluidized beds.

There are two possible reasons for such anomalous float–sink motions. The first is that the fluidized state of the bed is not uniform in space and time. Thus, the motion of the media particles, which changes instantaneously and locally, affects the motion of the immersed object. The second is that the presence of the immersed object alters the motion of the surrounding media particles. The motions of both air and the media particles are restricted around the surface of the object, inducing a local change in the fluidized state. Therefore, in addition to the hydrostatic pressure gradient, there is a pressure change attributed to the presence of the object, which exerts an additional force on the object. This is analogous to the “pressure drag” exerted on objects in fluid mechanics (Tsuji et al., 2022). For example, the differences in the float–sink motions of objects with different shapes, as described above, may be due to the second reason, i.e., changes in the pressure drag due to the object shape (Honda et al., 2023).

In recent years, our group has been investigating the float–sink motions of objects in gas–solid fluidized beds through experiments (Oshitani et al., 2016; Oshitani et al., 2023), numerical analyses (Tsuji et al., 2014; Tsuji et al., 2022), and measurements using a wireless sensor system (Harada et al., 2011; Higashida et al., 2016; Yoshimori et al., 2019; Uemoto et al., 2023). Regarding the measurements with a wireless sensor, many types of Lagrangian sensors, which is capsule-embedded MEMS sensors with a wireless module for the measurement of physical quantities following its motion, have developed for multiphase flows (Wadke et al., 2005; Shew et al., 2007; Gasteuil et al., 2007; Thiele et al., 2010; Sánchez-Colina et al., 2014; Bisgaard et al., 2020). Our group has also developed Lagrangian sensor systems to measure the vertical force acting on an object (Harada et al., 2011; Higashida et al., 2016), vertical position (Yoshimori et al., 2019), and orientation of a non-spherical object (Uemoto et al., 2023) in liquids and granular beds.

In this study, a new Lagrangian sensor was developed to measure the 3D position of objects in a fluidized bed, which cannot be observed from the outside. By extending the positional measurement to three dimensions, it became possible to visualize the object motion in the bed by computer graphics (CG). Using the developed sensor system, we investigated the similarity and dissimilarity between the float–sink motions of objects in fluidized beds and those in liquids, particularly when the object has the density close to the apparent density of the fluidized bed, at which anomalous motions are observed.

2. Experimental Method

2.1 Lagrangian sensor

In recent years, various methods for the measurement of internal motion in gas-solid fluidized beds have been proposed. Particularly, non-intrusive image acquisition techniques such as XCT (X-ray computational tomopgaphy), PET (positron emission tomopgaphy) and MRI (magnetic resonance imaging) (Errigo et al., 2024; van Buijtenen et al., 2011; Penn et al., 2017), and image analysis methods such as PTV (particle tracking velocimetry) and PIV (particle imaging velocimetry) have been rapidly developed (Ge et al., 2023; Neogi et al., 2023). However, these image acquisition methods are expensive and require large-scale equipments. On the other hand, wireless sensor systems have been developed to non-invasively measure the object motion in gas-solid fluidized beds. Although these systems are not able to measure the motion of media particles, they can track the motion of objects immersed in the fluidized bed from a Lagrangian viewpoint.

In this study, a Lagrangian sensor was employed to measure the 3D position of a spherical object in a gas–solid fluidized bed, which cannot be observed from the outside. In our previous studies, we developed a variety of Lagrangian sensors for various applications, including for the measurement of the force acting on a particle in a liquid (Harada et al., 2011), the simultaneous measurement of the vertical position and force acting on a spherical object in a fluidized bed (Yoshimori et al., 2019), and the angular measurement of a non-spherical object (Uemoto et al., 2023). In the present study, a new sensor system was developed to measure the 3D positions of an object in a gas–solid fluidized bed based on the previous Lagrangian sensor systems.

Figure 1 shows the appearance of the Lagrangian sensor particle. The sensing part comprises the same 9-axis motion sensor (InvenSense, MPU9250) used in the previous studies; however, for signal processing, a microcontroller board with Wi-Fi modules was employed (Switch Science, ESP-WROOM-02 developer board). The sensor and peripheral circuits were integrated onto a printed circuit board that was fabricated. The sensing part was placed in the center of a 40-mm-diameter outer spherical shell using a jig fabricated by a 3D printer. The motion sensor includes a 3-axis acceleration sensor, 3-axis magnetometer, and 3-axis gyroscope. As shown in Fig. 1, the sensor-mounted board is connected to the microcontroller board using integrated circuit pins. This facilitates handling, and the program in the microcomputer can be rewritten.

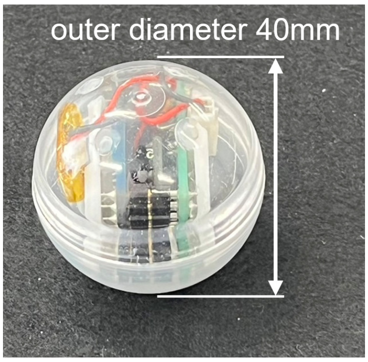

(a) outer appearance

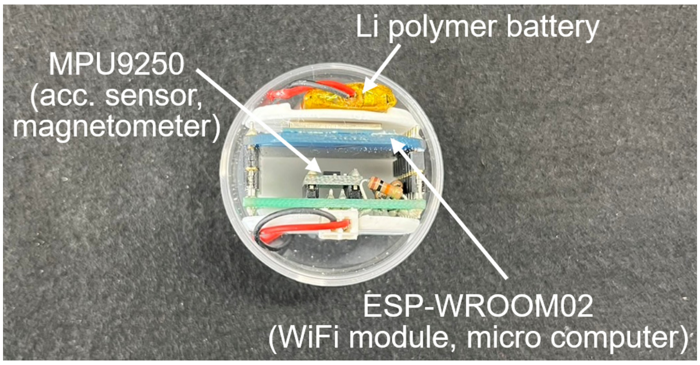

(b) inner appearance

Fig. 1 Appearance of the Lagrangian sensor particle.

Figure 2 represents the block diagram of the Lagrangian sensor system. The same power supply was used for all the sensors and the microcontroller in the Lagrangian sensor system. A lithium polymer battery (Data Power Technology Ltd., DTP401525) was used as the power source to provide a stable voltage. The voltage of the battery was 3.3 V, and the capacity was 110 mAh. The motion sensor was controlled by a microcontroller program, and control signals were sent via I2C communication. The output signals obtained from the sensor were serialized and sent to the receiver using the wireless module at a carrier frequency of 2.4 GHz. The microcontroller board with Wi-Fi modules (ESP-WROOM-32 developer board) was used as the signal receiver. This board controls the operation of the receiving side and is connected to a PC via USB. The serial monitor of the PC displays the measured signals simultaneously.

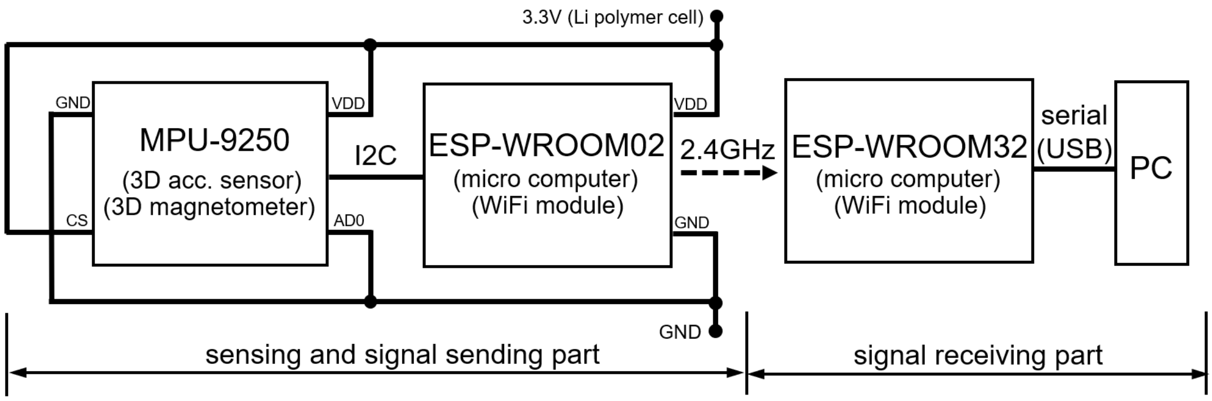

Fig. 2 Block diagram of the Lagrangian sensor system.

2.2 Three-dimensional Maxwell coil system

As described in the previous studies (Yoshimori et al., 2019; Uemoto et al., 2023), positional measurement with a Lagrangian sensor was achieved using a magnetic sensor to detect the magnetic vector from an externally applied gradient magnetic field. In this study, three pairs of gradient field coils (Maxwell coils) were installed for the 3D positional measurements. Figure 3 shows the appearance of the installed gradient field coils. Pairs of coils of the same size were installed in the *x*, *y*, and *z* directions, separately.

The coil diameter was 1100 mm, the distance between coils was 953 mm, and the number of coil turns was 163 in the *x* and *y* directions. The coil diameter in the *z* direction was 800 mm, the distance between coils was 693 mm, and the number of coil turns was 176. Linear magnetic fields with different magnitudes were generated at different locations by applying a current in the opposite

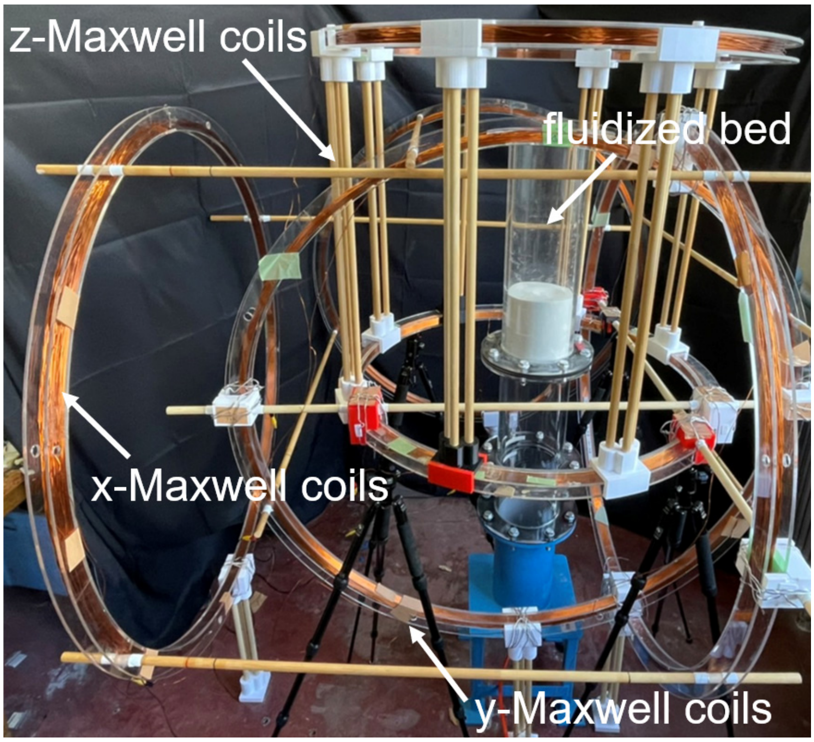

Fig. 3 Appearance of the 3D Maxwell coil system with the fluidized-bed apparatus. Horizontal direction (left to right) corresponds to *x* direction, direction from front to back is *y* direction and vertical direction is *z* direction.

direction to each coil. The voltage was DC 24 V, and the current in each coil was controlled by a variable resistor.

The linearity of the magnetic field generated by the gradient field coil is lost as one moves away from the central axis. The coils were arranged as shown in Fig. 3, with the center axis of each coil shifted to cover the measurement range of 150 mm × 150 mm × 150 mm. In the 3D measurement, each coil was switched on and off periodically using a relay switch, which is a device that can switch an electric circuit on and off using an external signal, to prevent interference between magnetic fields in each direction. The relay switch was controlled by a microcontroller board (Switch Science, Arduino Uno). The coil was switched on and off at 100 ms intervals by the microcontroller.

Figure 4 shows the relation between the averaged magnetic field strength and the position in each direction obtained by preliminary experiments. Based on these results, the calibration line for each position was obtained. As explained above, the magnitude of the magnetic vector varies as one moves away from the central axis. However, since the Lagrangian sensor moves freely in the

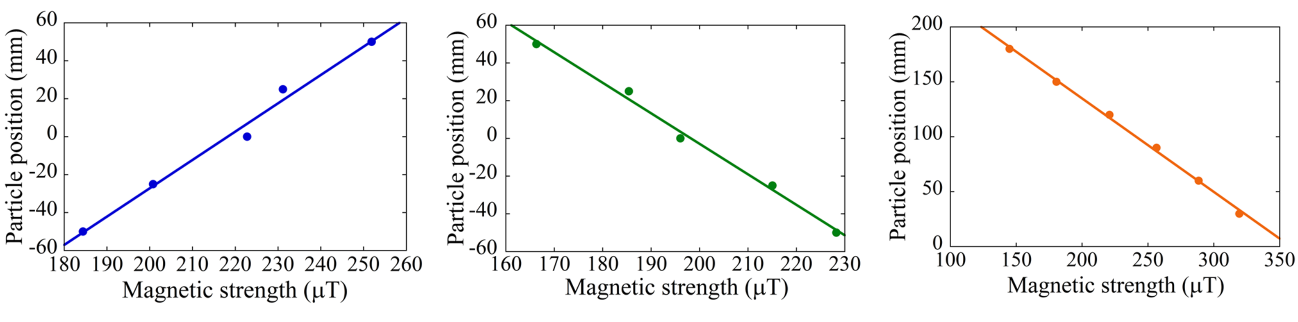

(a) *x* direction (b) *y* direction (c) *z* direction

Fig. 4 Calibration line of the gradient magnetic fields in each direction.

fluidized bed, it is not possible to switch the calibration line corresponding to the sensor position. Therefore, the calibration line was made by measuring the magnetic vectors at several points in each direction. The calibration lines in the x and y directions were made by measuring the magnetic field strength at five points (−50 mm, −25 mm, 0 mm, 25 mm, and 50 mm) at a vertical position of 90 mm. In the z direction, the magnetic strength was measured at six points at 30-mm intervals from the bottom of the fluidized bed.

As shown in Fig. 4, the calibration lines in each direction can be approximated as a linear function. Using these calibration lines, the 3D positions were obtained from the magnitude of the magnetic vector in each direction transmitted from an object (Lagrangian sensor) put into the gas–solid fluidized bed. As mentioned above, the switching of the magnetic field in each direction takes 100 ms. Thus, the time resolution of the 3D positional measurement was 300 ms.

The reliability of the Lagrangian sensor for positional measurement was confirmed in the previous study by harmonic vibration experiments (Yoshimori et al., 2019). In the previous experiment, the accuracy of position measurement in one direction was confirmed and it was within a few millimeters. As mentioned above, this study attempts to measure 3D positions of the object using three pairs of Maxwell coils. The basic accuracy is the same as in the previous study. However, since the linear gradient magnetic fields in x, y and z directions have to be overlapped, the magnetic error becomes larger at the edge of the measurement region. While the accuracy of the 3D Lagrangian measurement in this study is within a few millimeters in many locations, but the position error is about 10mm (1/4 of the object diameter) in some locations, especially at the corner of the fluidized bed.

2.3 Experimental setup of the fluidized bed

Figure 3 also shows the apparatus of the gas–solid fluidized bed placed at the center of the coil system. The apparatus has a cylindrical shape with a diameter of 150 mm. The media particles were glass beads with an average diameter of d_p = 150 μm and density of ρ_m = 2500 kg/m^3 (B-type particles in Geldart classification (Geldart, 1973)), which are the same as the particles used in the previous study (Honda et al., 2023). In the experiment, the media particles were filled to an initial layer height of 150 mm, and the Lagrangian sensor was placed statically at the center of the surface as a coarse object. Since the mass of the Lagrangian sensor caused it to dip slightly into the bed surface, the initial vertical position of the sensor particle was around 160–165 mm. After the Lagrangian sensor particle were placed, air was injected from the bottom to fluidize the media particles. The 3D position of the sensor particle was measured for 3 minutes after the start of the fluidization.

As is well-known, when the flow velocity u_0 exceeds the minimum fluidized velocity u_{mf}, the media particles are fluidized and the pressure difference supports the mass of media particles. In this case, the following pressure gradient occurs in the fluidized bed on average.

$$\frac{dp}{dz} = -\rho_m(1-\epsilon)g \tag{1}$$

where ρ_m is the density of media particles, g is the gravitational acceleration and ε is the void fraction. The above relation expresses the "hydrostatic pressure" in a gas–solid fluidized bed. Consequently, the corresponding "buoyant force" is exerted on the object immersed in the fluidized bed.

In the experiment, the air-inlet velocity u_0 was set to be close to the minimum fluidization velocity u_{mf} for u_0/u_{mf} = 1.2 ~ 1.5. Under these conditions, the particle bed was gently fluidized and expanded slightly. According to the measurement of the bed expansion, the void fraction after fluidization is approximately $\varepsilon = 0.44$ under these air-velocity conditions. As a result, the apparent density of the fluidized bed ρ_a (= ρ_m $(1-\varepsilon)$) is around 1400 kg/m^3.

Lead strips were inserted into the shell of the Lagrangian sensor particle and the object density was varied in the range of ρ_p = 910–1666 kg/m^3, with respect to the apparent density of the fluidized bed ρ_a. The insertion of lead does not guarantee that the center of gravity was exactly at the center of the objects. Accordingly, we note here that the effect of the angular motion of the object was not considered in this study.

3. Results and Discussion

3.1 Floating motion of low-density objects

Figure 5 shows the results of the 3D non-invasive measurements of the object positions in the gas–solid fluidized bed under the velocity condition of u_0/u_{mf} = 1.2 and at an object density of ρ_p =910 kg/m^3. As mentioned above, the apparent density of the fluidized bed under the present experimental conditions is around ρ_a = 1400 kg/m^3, which in principle corresponds to the condition where the object floats in the fluidized bed. Figure 6 presents a comparison between the observation images taken in the experiment and the CG-generated images from the Lagrangian measurements. The timing of both results is synchronized.

As shown in Fig. 6, the image taken from the outside only features objects above the surface of

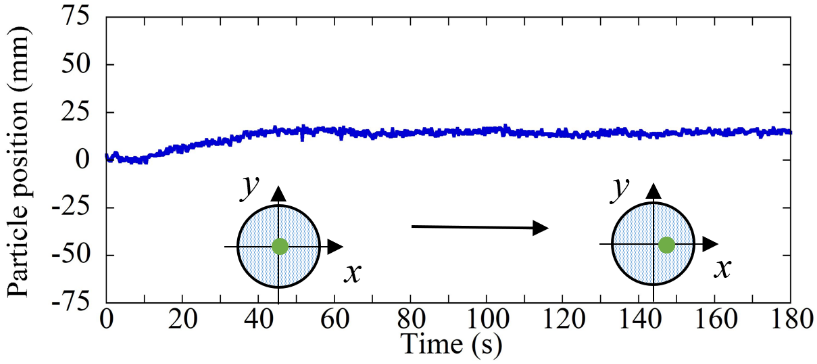

(a) x direction

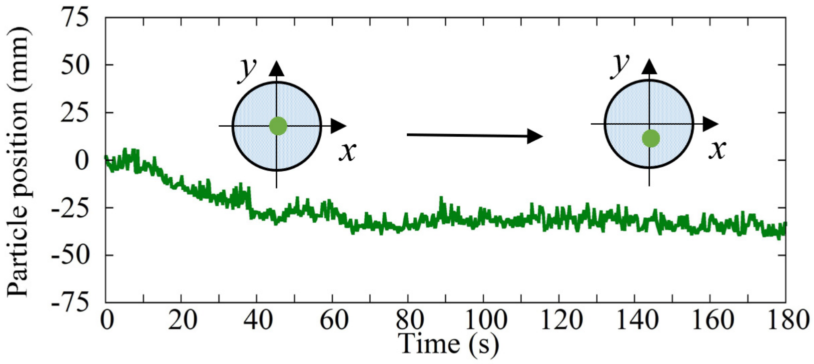

(b) y direction

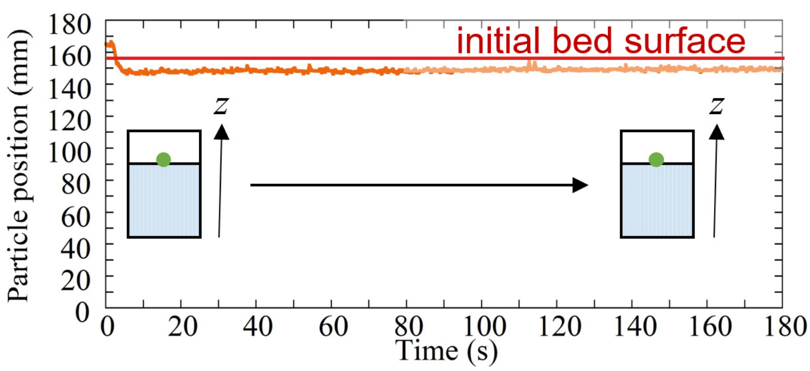

(c) z direction

Fig. 5 Measurement results of the 3D position of the Lagrangian sensor particle for ρ_p = 910 kg/m^3.

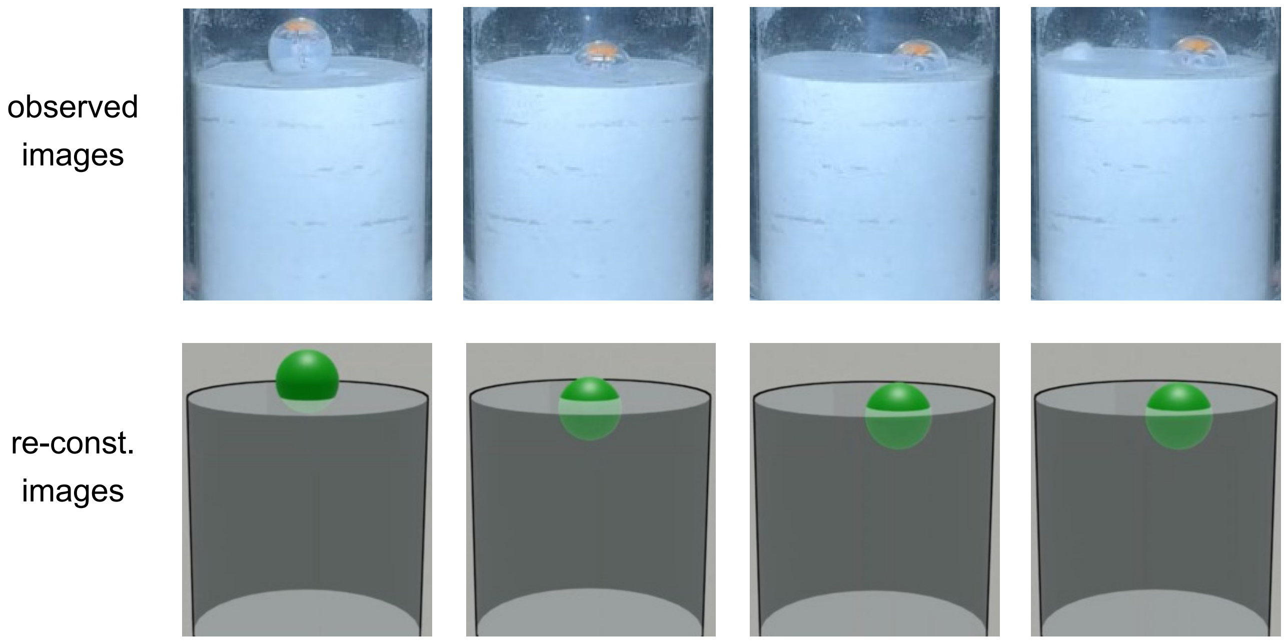

(a) t = 0 s (b) t = 6 s (c) t = 120 s (d) t = 180 s

Fig. 6 Observation and re-construction images from the Lagrangian measurement of the object motion for ρ_p = 910 kg/m^3; (upper) observed images, (lower) re-construction images. Horizontal direction (left to right) corresponds to x direction, direction from front to back is y direction and vertical direction is z direction.

the fluidized bed, whereas the CG images generated from the experimental results show the interior of the fluidized bed. The object behaviors at each time in the observation images are almost identical to those in the images generated from the measurement results. After the fluidization began, the Lagrangian sensor settles rapidly to a depth approximately equal to its radius, after which it floats near the surface of the bed. Figure 5 shows that the horizontal movement of the object is slightly positive and negative in the x and y directions, respectively. These behaviors are consistent with the experimental images shown in Fig. 6. The floating behavior of the object in the bed, as shown above, is similar to that in liquids. These results indicate that the media particles are suddenly "liquefied" once air is injected from the bottom and that the immersed object exerts buoyant force due to the hydrostatic-like pressure caused by the permeation resistance.

3.2 Sinking motion of high-density objects

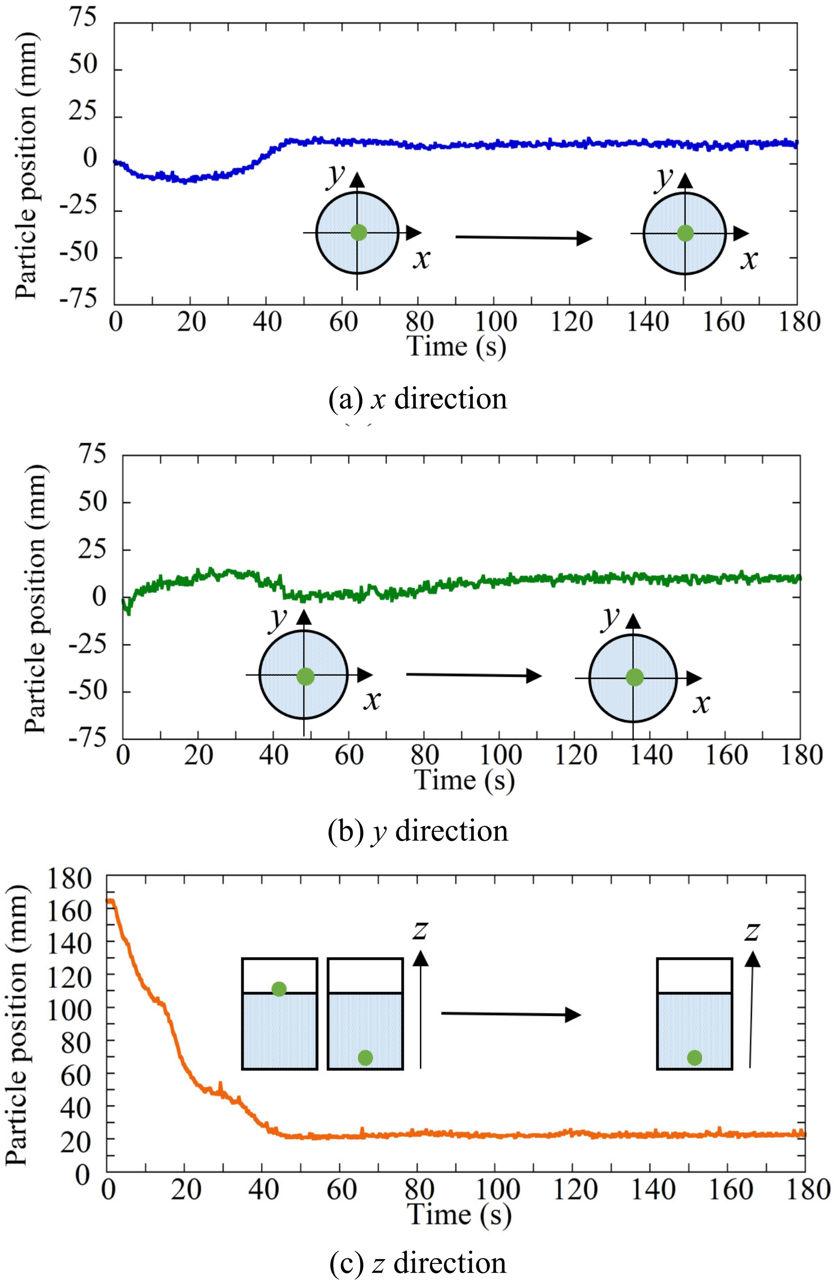

Fig. 7 Measurement results of the 3D position of the Lagrangian sensor particle for ρ_p = 1666 kg/m^3.

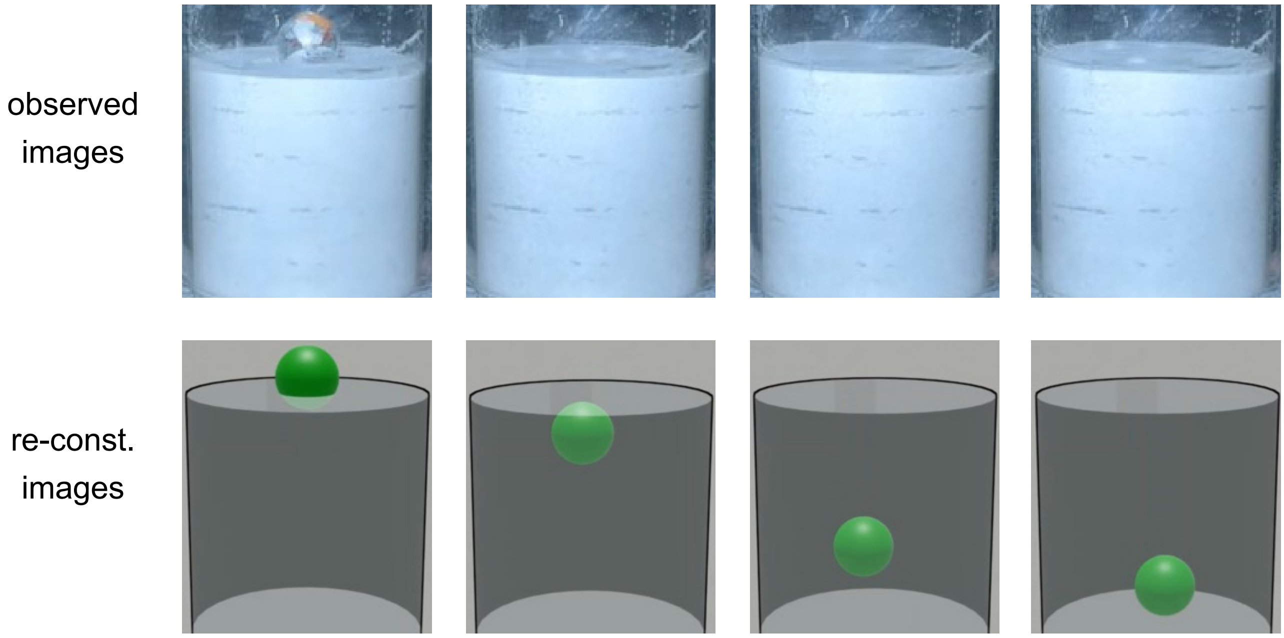

(a) $t = 0$ s (b) $t = 6$ s (c) $t = 24$ s (d) $t = 40$ s

Fig. 8 Observation and re-construction images from the Lagrangian measurement of the object motion for ρ_p = 1666 kg/m^3; (upper) observed images, (lower) re-construction images. Horizontal direction (left to right) corresponds to x direction, direction from front to back is y direction and vertical direction is z direction.

Figure 7 shows the results of the 3D measurements of the object positions in the fluidized bed for the object density of ρ_p = 1666 kg/m^3. The conditions in the fluidized bed are the same as those in the previous section. In this case, the object density is higher than the apparent density of the fluidized bed, which, in principle, corresponds to a condition where the object sinks to the bottom of the fluidized bed.

Figure 8 presents a comparison between the observation images and the CG images generated from the Lagrangian measurement results. In the observation image, the object quickly becomes invisible after fluidization, whereas the object behavior inside the fluidized bed can be clearly understood in the images generated from the measurement results. After fluidization begins, the object is rapidly buried in the fluidized bed, after which it moves downward near the center of the fluidized bed at an almost constant velocity over a period of about 20 seconds. The object moves slightly horizontally and subsequently returns to the center. Additionally, as shown in Fig. 7(c), the object slows down just before it lands at the bottom of the bed and behaves as if it is slightly lifted off (20–40 s). As will be discussed later, this is thought to be due to the influence of the void layer that is constantly present near the bottom of the fluidized bed.

As shown in the observation image, small bubbles are generated on the surface of the fluidized bed after the object sinks (Fig. 8d). This is caused by the local fluidization of media particles near the surface of the object remaining at the bottom of the bed. The slow sinking of objects in the fluidized bed, as shown in Fig. 8, appears to indicate the dissimilarity between the fluidized bed and liquids. A detailed description of the settling velocity of objects will be provided later.

3.3 Anomalous motion of moderate-density objects

Figure 9 shows the results of the 3D measurements of the object positions in the fluidized bed at an object density of ρ_p = 1350 kg/m^3. This object density is approximately equal to the apparent density of the fluidized bed. Figure 10 shows a comparison between the observation image and the CG image generated from the measurement results. As shown in Figs. 9 and 10, the object settles at a depth approximately equal to its radius in a few seconds after fluidization and subsequently stagnates. However, after stagnating for about 100 seconds, the object moves downward again. In the observation image, the object is buried in the fluidized bed and becomes invisible after 120 seconds. In the CG-generated image, however, the object can be observed to be sinking in the fluidized bed at a very low velocity. The appearance of objects on the surface of the fluidized bed is slightly different between the observation image and the CG-generated image. This may be caused by the slight expansion of the fluidized bed in the experiment. These sinking behaviors described

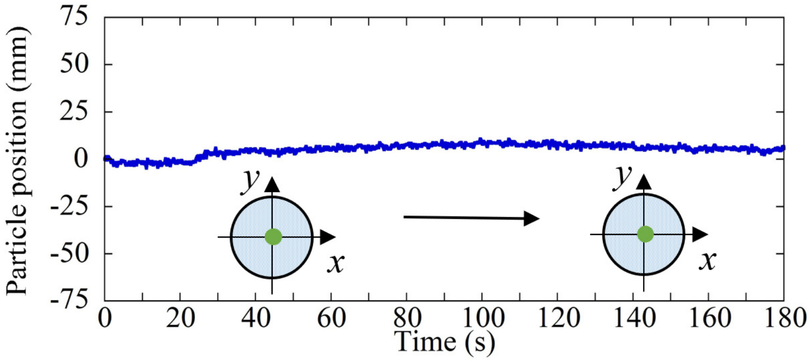

(a) x direction

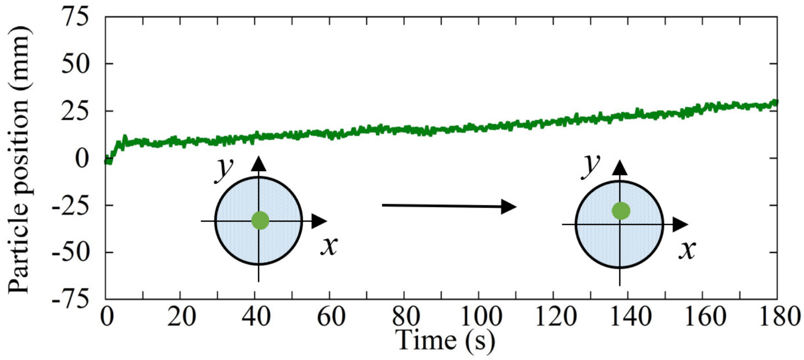

(b) y direction

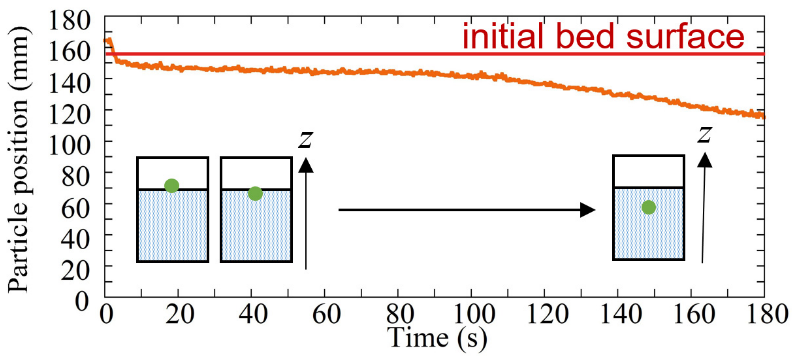

(c) z direction

Fig. 9 Measurement results of the 3D position of the Lagrangian sensor particle for ρ_p = 1350 kg/m^3.

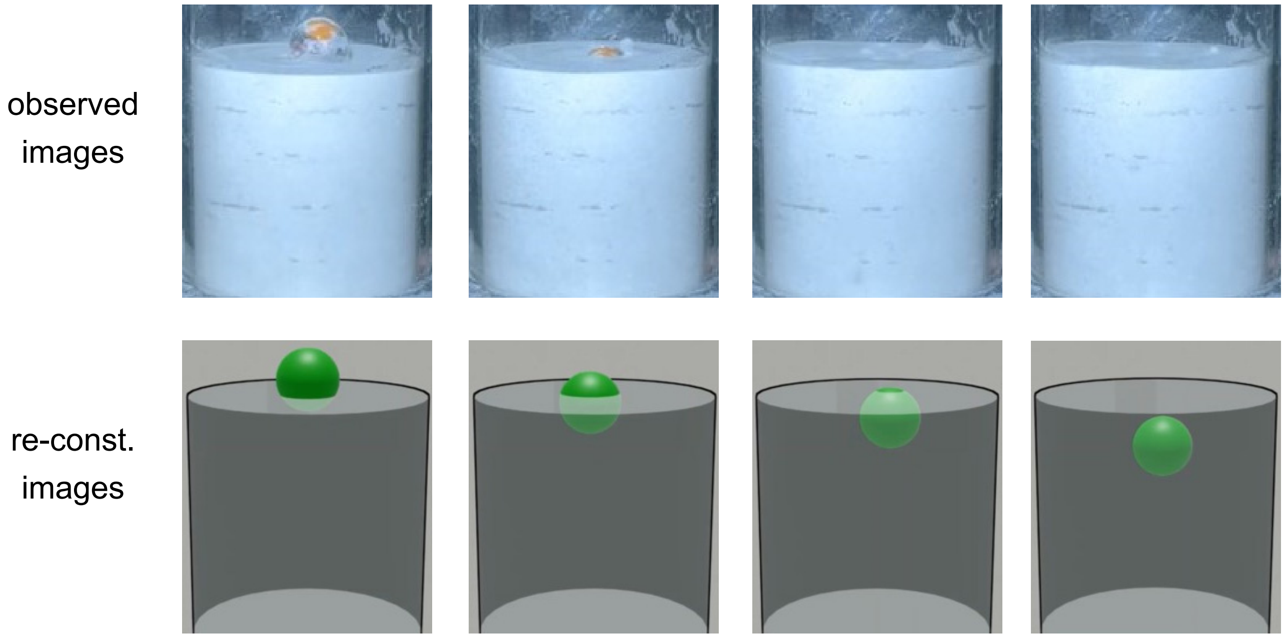

(a) t = 0 s (b) t = 6 s (c) t = 120 s (d) t = 180 s

Fig. 10 Observation and re-construction images from the Lagrangian measurement of the object motion for ρ_p = 1350 kg/m^3; (upper) observed images, (lower) re-construction images. Horizontal direction (left to right) corresponds to x direction, direction from front to back is y direction and vertical direction is z direction.

above, where the object stagnates near the surface of the fluidized bed for a few minutes and subsequently settles down again, is unthinkable in liquid, indicating the dissimilarity of float–sink motions in fluidized beds to those in liquids.

3.4 Detailed vertical motion in the fluidized bed

The details of incomprehensive behaviors of objects with a density close to the apparent density of fluidized bed were examined. Figure 11 shows the final vertical position of the object measured by the Lagrangian sensor under the air velocity condition of u_0/u_{mf} = 1.5. In these experiments, we measure only the vertical position of objects using z-magnetic coils. Following the float–sink

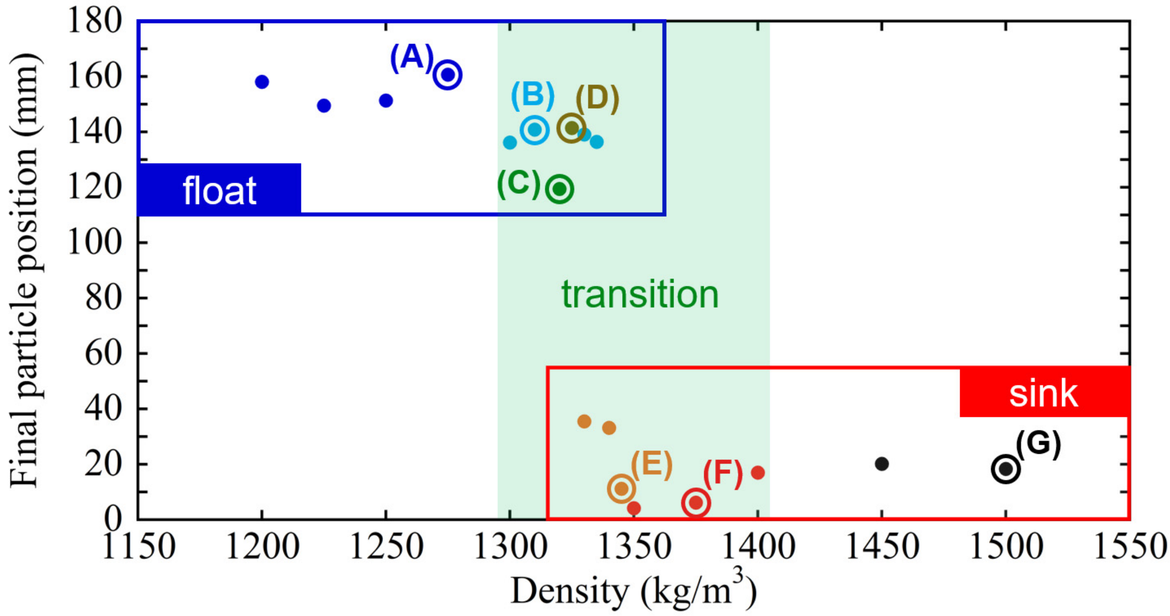

Fig. 11 Final vertical position of the object in the gas–solid fluidized bed for $u_0/u_{mf} = 1.5$.

principle described above, when the object density is lower than the apparent density of the fluidized bed, the object floats on the surface layer. In contrast, when the object density is higher than the apparent density, the object sinks to the bottom of the bed. However, when the object density is similar to the apparent density, the object may stagnate inside the fluidized bed or its final position may differ even under the same density conditions, resulting in ambiguous behaviors with poor reproducibility. Hereinafter, we focus on conditions (A)–(G) in Fig. 11, which represent the typical float–sink motions, to examine the changes in the vertical position.

Figure 12 represents the temporal change of vertical position of the object in the fluidized bed under conditions of (A)–(G), which was measured by Lagrangian sensor system. As described in each figure, the settling behavior of objects categorized into four stages, i.e., (I) initial rapid settling, (II) gradual settling, (III) rapid sinking, and (IV) complex landing at the bottom of the bed. Hereafter, the object behavior under each condition is discussed in detail.

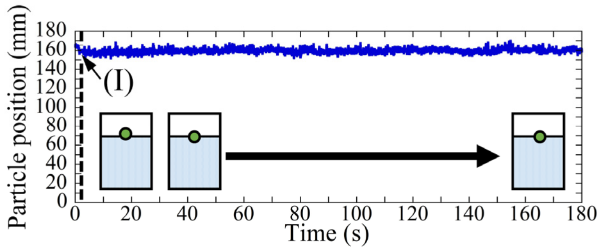

(A) ρ_p = 1275 kg/m^3

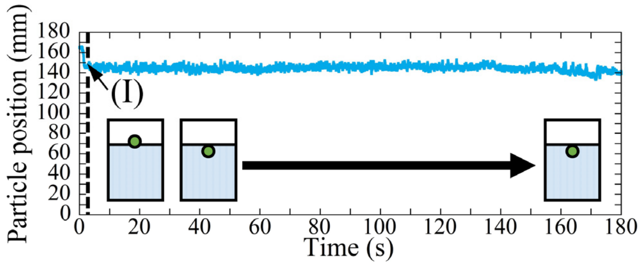

(B) ρ_p = 1310 kg/m^3

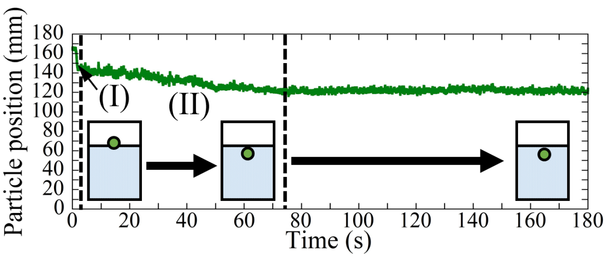

(C) ρ_p = 1320 kg/m^3

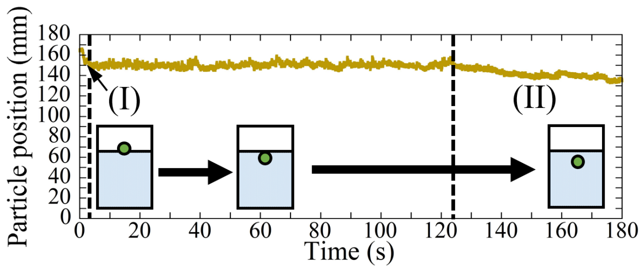

(D) ρ_p = 1325 kg/m^3

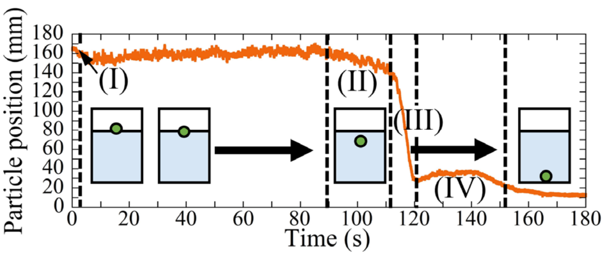

(E) ρ_p = 1345 kg/m^3

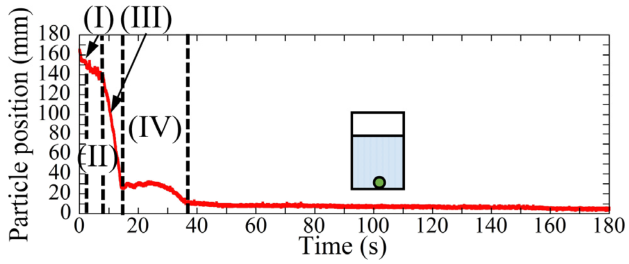

(F) ρ_p = 1375 kg/m^3

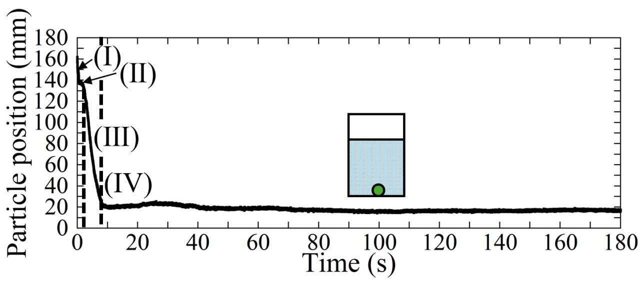

(G) ρ_p = 1500 kg/m^3

Fig. 12 Vertical motion of the object measured by the Lagrangian sensor system for conditions (A)–(G). (I)–(IV) in each figure indicate the settling stages, i.e., (I) initial rapid settling, (II) gradual settling, (III) rapid sinking, and (IV) complex landing, respectively.

Figure 12 (A) shows the change in the vertical position of the object in the fluidized bed for the object density of ρ_p = 1275 kg/m^3. As shown above, when the object density is adequately lower than the apparent density of the fluidized bed, the particles sink rapidly to a depth equal to the particle radius, after which they stagnate near the surface of the bed. All objects with densities below ρ_p = 1275 kg/m^3 exhibited such vertical motions. Conversely, the results shown in Fig. 12 (B) are for objects with a density of ρ_p = 1310 kg/m^3. Compared with the result in (A), the object sinks deeply inside the fluidized bed. As shown in Fig. 12, at object densities close to the apparent density of the fluidized bed, the stagnation position of the object moves downward. Although the difference of the object density is only a few tens of kg/m^3, the stagnation position moves approximately 10–20 mm downward compared with the case when the density is sufficiently small.

At object densities near the apparent density of the fluidized bed, a variety of float–sink behaviors are observed. Fig. 12 (C) shows the change in the vertical position of the object at the density of ρ_p = 1320 kg/m^3. Under this condition, after rapid initial settling at the start of fluidization, the object settles very slowly in approximately 70–80 seconds. After that, the object stops moving and stagnates. Furthermore, under the condition of ρ_p = 1325 kg/m^3, as shown in Fig. 12 (D), after the initial rapid settling, the object stops moving and stagnates for 120 seconds, after which it begins to settle at a very low velocity. Thus, at object densities close to the apparent density of the fluidized bed, even if the final vertical position is the same, the vertical motions of the objects is anomalous in a way that are unimaginable in liquids. Under such density conditions, the reproducibility of object motion is poor, and a slight change in the motion of media particles may trigger a change in the object motion.

Fig. 12 (E) shows the change in the vertical position of the object at the density of ρ_p = 1345 kg/m^3. As shown in the figure, after the initial rapid settling, the object stagnates near the surface for approximately 80 seconds. Then it begins to settle slowly for 20 seconds. After that, it sinks rapidly when the vertical position exceeds 120 mm and reaches near the bottom. Afterward, the object floats near the bottom, and subsequently lands gently at the bottom of the fluidized bed.

Fig. 12 (F) shows the experimental results obtained at the object density of ρ_p = 1375 kg/m^3. As was the case under the other density conditions, the object settles rapidly after the start of fluidization, settles gently, settles rapidly again, and finally lands softly at the bottom of the bed, similar to the behaviors observed under condition (E). At object densities higher than those for condition (F), the object behaves similarly to the object under condition (F), i.e., more continuous settling to the bottom immediately after the start of fluidization. Fig. 12 (G) shows the results at ρ_p = 1500 kg/m^3, which is adequately larger than the apparent density. In this case, the object settles immediately into the bottom, therefore the object trajecroty is almost linearly with time.

As indicated above, the float–sink motions of objects with densities close to the apparent density of the fluidized bed are complicated and remarkably dissimilar compared with those in liquids. These results suggest that the object motion in a fluidized bed is somewhat position-dependent.

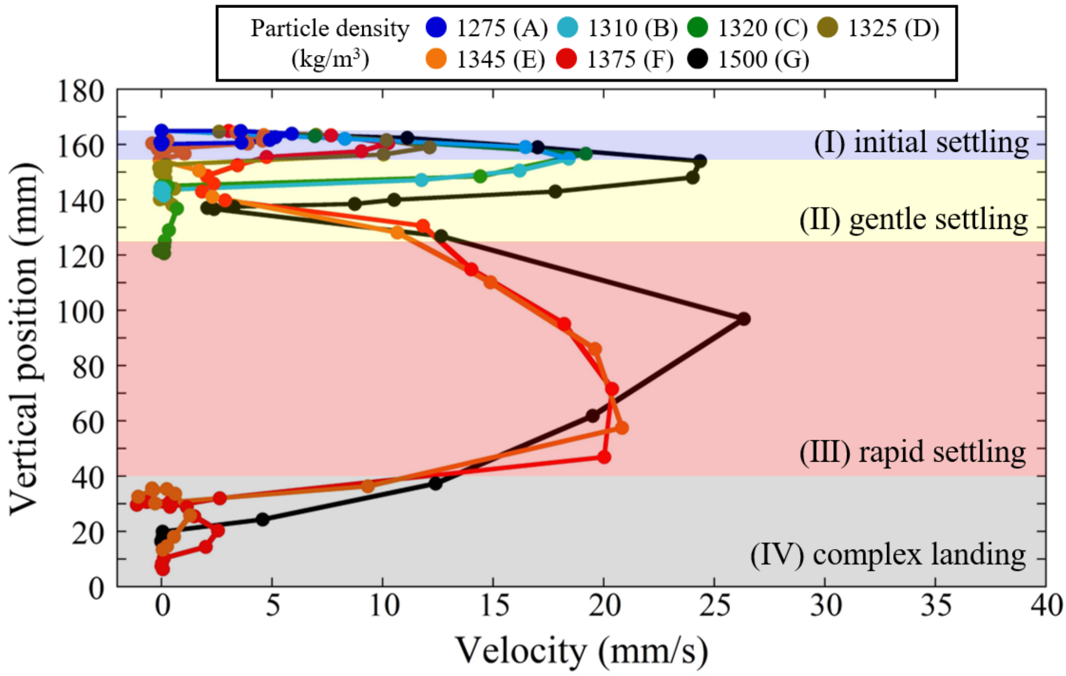

Fig. 13 Relation between the vertical position and the settling velocity of the object.

Figure 13 shows the relation between the vertical position and settling velocity of objects for conditions (A)–(G). The object velocity was obtained by a local linear approximation of the time variation of the object position shown in Fig. 12. Based on velocity changes, the settling stages can be understood more clearly, i.e., (I) initial rapid settling, (II) gradual settling, (III) rapid sinking, and (IV) complex landing. As shown in Fig. 13, these stages occur at specific vertical positions in the fluidized bed.

The initial settling region (Stage I) is about 10 mm from the surface, and the settling velocity ranges from 5 to 30 mm/s. This wide range of the initial settling velocity is probably due to the fact that when the fluidization of the media particles starts, the bed surface does not liquefy uniformly because of spatial variations in airflow. As shown in Fig. 12, the settling velocity in Stage I varies independently on the object density, because it depends greatly on the behavior of the media particles just after fluidization. By the inlet of airflow, the ground below the object changes from compacted and hard one to "liquefied" one for a very short time (on the order of 0.1s). However, the liquefaction does not occur uniformly. The settling velocity of the object in Stage I varies depending on whether the ground is instantly liquefied or a gradual change to a liquid-like state.

In the gentle settling region (Stage II), the object velocities are less than 5 mm/s under all density conditions. This may be due to the presence of a large barrier around the bed height of 120 mm. Under the low-density conditions (A)–(C), the objects are trapped by the barrier and consequently stagnate near the surface. In Stage II, the object moves downward, albeit against considerable resistance. Under conditions (C) and (D), the object moves downward in Stage II at a very low velocity. This gradual change in position may be due to the local fluidization around the object.

The objects that break through the barrier in Region (II) settle rapidly in Region (III). As shown in Fig. 12, the object settles at an approximately constant velocity in this region. This implies that a viscous-like resistance force may acts to determine the settling velocity, analogous to Stokes settling velocity in liquids. However, the factors that determine the object velocity in Stage III are not covered in the present study, because of insufficient experimental data.

In Stage IV, the object tends to land gently at the bottom once its velocity decreases. As is well-known, a high void layer is found just above the bottom of the fluidized bed. Therefore, the object is retarded by additional resistance due to the influence of the inlet airflow when it enters the high void region. Hoewver, if the object density is adequately larger than the apparent density (condition (G)), this effect is minor as shown in Fig.13.

Thus, there are two vertical barriers in the fluidized bed for objects, i.e., the barrier near the bed surface and the barrier near the bottom of the bed. As mentioned above, the lower barrier is obviously due to the influence of high void region at the bottom of the bed. There are two possible explanations for the upper barrier: 1) a change in the fluidized state of the media particles near the surface and 2) an object-size dependent barrier, i.e., an increase in the resistance because the object is not fully submerged in the media particles. In this experiment, we could not change the size of the object because of the size of the sensor system. However, future experiments with different object sizes will clarify the mechanism of the upper barrier in the fluidized bed.

4. Conclusions

The 3D non-invasive measurement of the float–sink motions of coarse objects in a gas–solid fluidized bed was conducted. A new wireless sensor system was developed for the measurement of the object positions in the fluidized bed, which cannot be observed from the outside. Spherical objects were used and the object density was adjusted on the basis of the apparent density of the fluidized bed. Experiments were conducted with varying the densities of the objects, specifically within ranges close to the apparent density of the fluidized bed, to investigate the details of their float–sink behaviors in the fluidized bed.

By extending the measurement to three dimensions, it was possible to visualize the details of the object motion in the bed by CG. The experimental results showed that the float–sink motions of objects in the gas–solid fluidized bed are not similar to those in liquids, particularly at object densities close to the apparent density of the fluidized bed. The object velocity in the bed varied complicatedly depending on the vertical position. There are two barriers for the objects in the vertical direction, i.e., the barrier near the bed surface and the barrier near the bottom of the bed. At least, the ability to break through the upper barrier determines whether the object can reach the bottom of the fluidized bed. In conclusion, the float–sink motions of objects in gas–solid fluidized beds are complex and differ markedly from those in liquids.

This is the first 3D measurement we have successfully performed using the Lagrangian sensor system. Compared to the other non-invasive methods, such as XCT and PET, this method has the advantage of being an inexpensive measurement of object motion which can not be observed from outside. We are currently developing a smaller Lagrangian sensor of about 20 to 30 mm. However, 3D Lagrangian measurements require delicate positioning of the three pairs of coils, as well as many careful preparations such as switching the current at high speed using relay switches. Therefore, 3D measurements have yet to be realized under limited conditions at present. By brushing up the measurement system, it will be possible to directly detect the minute movements of objects in the fluidized bed, including in the horizontal direction, and to elucidate the mechanism of the barriers in the bed.

Conflict of Interest

The authors declare that there is no conflict of interest.

Acknowledgment

A part of this study was supported by JSPS KAKENHI Grant Number JP21H03646.

References

[1] Bisgaard, J., Muldbak, M., Cornelissen, S., Tajsoleman, T. Huusom, J. K., Rasmussen. T. and Gernaey, K. V., Flow-following sensor devices: a tool for bridging data and model predictions in large-scale fermentations, *Comp. Str. Biotech. J.*, 18 (2020) 2908–2919.

[2] Chen, X., Zhong, W. and Heindel, T. J., Orientation of cylindrical particles in a fluidized bed based on stereo X-ray particle tracking velocimetry (XPTV), *Chem. Eng. Sci.,* 203 (2019) 104–112.

[3] Chen, X., Zhong, W. and Heindel, T. J., Using stereo XPTV to determine cylindrical particle distribution and velocity in a binary fluidized bed, *AIChE J.,* 65 (2019) 520–535.

[4] Errigo, M. Windows-Yule, C., Materazzi, M., Werner, D. and Lettieri, P., Non-invasive and non-intrusive diagnostic techniques for gas-solid fluidized beds –A review, *Powder Technol.*, 431 (2024) 119098.

[5] Fotovat F., Chaouki J. and Bergthorson, J., Distribution of large biomass particles in a sand-biomass fluidized bed: experiments and modeling, *AIChE J.,* 60 (2014) 869–880.

[6] Gasteuil, Y., Shew, W. L., Gibert, M., Chillá, F., Castaing, B. and Pinton, J.-F., Lagrangian temperature, velocity, and local heat flux measurement in Rayleigh-Bénard convection, *Phys. Rev. Lett.*, 99 (2007) 234302.

[7] Ge, M,. Zhou, H., Vaidheeswaran, A., Rogers, W., Fan, D. and Li, C., Multi-scale experimental investigation on the fluidization of Geldart B 13X zeolite particles: A comprehensive dataset for CFD calidation, *Chem. Eng. J.*, 471 (2023) 144724.

[8] Geldart, D., Types of gas fluidization, *Powder Technol.*, 7 (1973) 285–292.

[9] Goldhirsch, I., Rapid granular flows, *Annu. Rev. Fluid Mech*., 35 (2003) 267–293.

[10] Harada, S., Kobayashi, Y., Sawano, T. and Noguchi, E., Direct measurement of fluid force on a particle in liquid by telemetry system, *Int. J. Multiphase Flow*, 37 (2011) 898–905.

[11] Higashida, K., Rai, K., Yoshimori, W., Ikegai, T., Tsuji, T., Harada, S., Oshitani, J. and Tanaka, T., Dynamic vertical forces working on a large object floating in gas-fluidized bed: discrete particle simulation and Lagrangian measurement, *Chem. Eng. Sci.*, 151, (2016) 105–115.

[12] Honda, Y., Saito, S., Anzai, T., Harada, S., Tsuji, T., Washino, K., Oshitani, J., Kajiwara, H. and Matsuoka, K., Experimental verification of the Brinkman equation around objects with various shapes in gas–solid stationary and fluidized beds, *Int. J. Multiphase Flow*, 160 (2023) 104359.

[13] Kunii, D. and Levenspiel, O., Fluidization Engineering, 2nd ed., (1991) Butterworth-Heinemann, Boston.

[14] Neogi, A., Mohanta, H. K. and Sande, P. C., Particle image velocimetry investigations on multiphase flow in fluidized beds: A review, *Flow Meas. Instrum*., 89 (2023) 102309.

[15] Oshitani, J., Kajimoto, S., Yoshida, M., Franks, G. V., Kubo, Y. and Nakatsukasa, S., Continuous float–sink density separation of lump iron ore using a dry sand fluidized bed dense medium, *Adv. Pow. Tech.,* 24 (2013) 468–472.

[16] Oshitani, J., Ohnishi, M., Yoshida, M., Franks, G. V., Kubo, Y. and Nakatsukasa, S., Dry separation of particulate iron ore using density-segregation in a gas-solid fluidized bed, *Adv. Pow. Tech.*, 24 (2013) 554–559.

[17] Oshitani, J., Sasaki, T., Tsuji, T., Higashida, K. and Chan, D. Y. C., Anomalous sinking of spheres due to local fluidization of apparently fixed powder beds, *Phys. Rev. Lett.*, 116 (2016) 068001.

[18] Oshitani, J., Kato, S., Tsuji, T., Washino, K., Harada, S., Sakamoto, Y., Kajiwara, H., Matsuoka, K. and Franks, G. V., Influence of air velocity and powder bed height on local density in a gas–solid fluidized bed and float–sink of spheres, *Adv. Pow. Tech.*, 34 (2023), 104146.

[19] Penn, A., Tsuji, T., Brunner, D. O., Boyce, C. M., Pruessmann, K. P. and Müller, C. R., Real-time probing of granular dynamics with magnetic resonance**,** *Sci. Adv.*, 3 (2017) e1701879.

[20] Sánchez-Colina, G., Alonso-Llanes, L., Martínez, E., Batista-Leyva, A. J., Clement, C., Fliedner, C., Toussaint, R. and Altshuler, E., Note: “Lock-in accelerometry” to follow sink dynamics in shaken granular matter, *Rev. Sci. Instrum.*, 85 (2014) 126101.

[21] Shew, W. L., Gasteuil, Y., Gibert, M., Metz, P. and Pinton, J.-F., Instrumented tracer for Lagrangian measurements in Rayleigh-Bénard convection, *Rev. Sci. Instrum.*, 78 (2007) 065105.

[22] Soria-Verdugo, A., Garcia-Gutierrez, L. M., Garcia-Hernando, N. and Ruiz-Rivas, U., Buoyancy effects on objects moving in a bubbling fluidized bed, Chem. Eng. Sci., 66 (2011) 2833–2841.

[23] Thiele, S., Silva, J.D. and Hampel, U., Autonomous sensor particle for parameter tracking in large vessels, *Meas. Sci. Technol.,* 21 (2010) 085201.

[24] Tsuji, T., Higashida, K., Okuyama, Y. and Tanaka, T., Fictitious particle method: a numerical model for flows including dense solids with large size difference, *AIChE J.,* 60 (2014) 1606–1620.

[25] Tsuji, T., Penn, A., Hattori, T., Pruessmann, K. P., Müller, C.R., Oshitani, J., Washino, K. and Tanaka, T., Mechanism of anomalous sinking of an intruder in a granular packing close to incipient fluidization, *Phys. Rev. Fluids*, 6 (2021) 064305.

[26] Tsuji, T., Sakamoto, Y., Harada, S., Uemoto, K., Oshitani, J., Washino, K., Tanaka, T., Kajiwara, H. and Matsuoka, K., FPM-SE: a numerical model for dense gas-solid flows with large non-spherical object, *Chem. Eng. Sci.*, 264 (2022) 118149.

[27] Uemoto, K., Narita, S., Harada, S., Sakamoto, Y., Tsuji, T., Oshitani, J., Kajiwara, H. and Matsuoka, K., Wireless measurement of float–sink motion of variously-shaped objects in gas–solid fluidized bed, *Adv. Pow. Tech.*, 34 (2023), 104111.

[28] van Buijtennen, M. S., van Dijk, W.-J., Deen, N. G., Kuipers, J. A. M., Leadbeater, T. and Parker, D. J., Numerical and experimental study on multi-spout fluidized beds, *Chem. Eng. Sci.*, 66 (2011) 2368–2376.

[29] Wadke, P. M., Hounslow, M. J. and Salman A. D., The ‘smart’ sphere, experimental results, *Chem. Eng. Res. Des.*, 83 (2005) 1298–1302.

[30] Yoshimori, W., Ikegai, T., Uemoto, K., Narita, S., Harada, S., Oshitani, J., Tsuji, T., Kajiwara, H. and Matsuoka, K., Non-invasive measurement of floating-sinking motion of a large object in a gas-solid fluidized bed, *Gran. Matt.*, 21 (2019) 1–11.